University of Kent

Kent Academic Repository

Buey, Rubén M., Mohan, Renu, Leslie, Kris D., Walzthoeni, Thomas, Missimer, John H., Menzel, Andreas, Bjelić, Saša, Bargsten, Katja, Grigoriev, Ilya, Smal, Ihor and others (2011) ***Insights into EB1 structure and the role of its C-terminal domain for discriminating microtubule tips from the lattice.*** **Molecular Biology of the Cell, 22 (16). pp. 2912-2923. ISSN 1059-1524.**

Downloaded from

https://kar.kent.ac.uk/115051/ The University of Kent's Academic Repository KAR

The version of record is available from

https://doi.org/doi:10.1091/mbc.E11-01-0017

This document version

Publisher pdf

DOI for this version

Licence for this version

UNSPECIFIED

Additional information

Versions of research works

Versions of Record

If this version is the version of record, it is the same as the published version available on the publisher's web site. Cite as the published version.

Author Accepted Manuscripts

If this document is identified as the Author Accepted Manuscript it is the version after peer review but before type setting, copy editing or publisher branding. Cite as Surname, Initial. (Year) 'Title of article'. To be published in ***Title of Journal*** , Volume and issue numbers [peer-reviewed accepted version]. Available at: DOI or URL (Accessed: date).

Enquiries

If you have questions about this document contact ResearchSupport@kent.ac.uk. Please include the URL of the record in KAR. If you believe that your, or a third party's rights have been compromised through this document please see our Take Down policy (available from https://www.kent.ac.uk/guides/kar-the-kent-academic-repository#policies).

Insights into EB1 structure and the role of its C-terminal domain for discriminating microtubule tips from the lattice

Rubén M. Buey[a,*], Renu Mohan[b,†], Kris Leslie[b], Thomas Walzthoeni[c,d], John H. Missimer[a], Andreas Menzel[e], Saša Bjelić[a], Katja Bargsten[a], Ilya Grigoriev[b,†], Ihor Smal[f], Erik Meijering[f], Ruedi Aebersold[c,g,h], Anna Akhmanova[b,†], and Michel O. Steinmetz[a]

[a]Biomolecular Research, Paul Scherrer Institut, 5232 Villigen PSI, Switzerland; [b]Department of Cell Biology, Erasmus Medical Center, Rotterdam 3000 CA, Netherlands; [c]Institute of Molecular Systems Biology, ETH Zürich, 8093 Zürich, Switzerland; [d]Ph.D. Program in Molecular Life Sciences, University of Zürich/ETH Zürich, 8093 Zürich, Switzerland; [e]Synchrotron Radiation and Nanotechnology, Paul Scherrer Institut, 5232 Villigen PSI, Switzerland; [f]Biomedical Imaging Group Rotterdam, Department of Medical Informatics and Radiology, Erasmus Medical Center, Rotterdam 3000 CA, Netherlands; [g]Faculty of Science, University of Zürich, 8093 Zürich, Switzerland; [h]Competence Center for Systems Physiology and Metabolic Diseases, 8093 Zürich, Switzerland

ABSTRACT **End-binding proteins (EBs) comprise a conserved family of microtubule plus end–tracking proteins. The concerted action of calponin homology (CH), linker, and C-terminal domains of EBs is important for their autonomous microtubule tip tracking, regulation of microtubule dynamics, and recruitment of numerous partners to microtubule ends. Here we report the detailed structural and biochemical analysis of mammalian EBs. Small-angle X-ray scattering, electron microscopy, and chemical cross-linking in combination with mass spectrometry indicate that EBs are elongated molecules with two interacting CH domains, an arrangement reminiscent of that seen in other microtubule- and actin-binding proteins. Removal of the negatively charged C-terminal tail did not affect the overall conformation of EBs; however, it increased the dwell times of EBs on the microtubule lattice in microtubule tip–tracking reconstitution experiments. An even more stable association with the microtubule lattice was observed when the entire negatively charged C-terminal domain of EBs was replaced by a neutral coiled-coil motif. In contrast, the interaction of EBs with growing microtubule tips was not significantly affected by these C-terminal domain mutations. Our data indicate that long-range electrostatic repulsive interactions between the C-terminus and the microtubule lattice drive the specificity of EBs for growing microtubule ends.**

Monitoring Editor
Gero Steinberg
University of Exeter

Received: Jan 7, 2011
Revised: May 12, 2011
Accepted: Jun 16, 2011

This article was published online ahead of print in MBoC in Press (http://www.molbiolcell.org/cgi/doi/10.1091/mbc.E11-01-0017) on July 7, 2011.

A.A. and M.O.S. contributed equally to this work.

Present addresses: *Centro de Investigación del Cáncer, Universidad de Salamanca–Consejo Superior de Investigaciones Cientificas, 37007 Salamanca, Spain; †Cell Biology, Faculty of Science, Utrecht University, Utrecht 3584 CH, Netherlands.

Address correspondence to: Rubén M. Buey (ruben.martinez@usal.es), Michel O. Steinmetz (michel.steinmetz@psi.ch).

Abbreviations used: AU, arbitrary unit; buf, buffer; Cα, alpha carbon; CCD, charge-coupled device; CH, calponin homology; C-ter, C-terminal; DAPI, 4′,6-diamidino-2-phenylindol; Dmax, maximum particle distance; DSS, disuccinimidyl suberate; EB, end binding protein; EBH, EB-homology; EGF, epidermal growth factor; EGFR, epidermal growth factor receptor; EGTA, ethylene glycol tetraacetic acid; FRAP, fluorescence recovery after photobleaching; GFP, green fluorescent protein; GMPCPP, guanosine-5′-[(α, β) -methyleno]triphosphate; GTP, guanosine-5′-triphosphate; LZ, leucine zipper; MAP, microtubule-associated protein; MS, mass spectrometry; MT, microtubule; PDB, Protein Data Bank; PDF, pair distribution function; PIPES, 1,4-piperazinediethanesulfonic acid; Rg, radius of gyration; SAXS, small-angle x-ray scattering; SEC, size exclusion chromatography; TEM, transmission electron microscopy; +TIP, microtubule plus end–tracking protein; TIRFM, total internal reflection fluorescence microscopy; Tris, Tris(hydroxymethyl)aminomethane.

© 2011 Buey *et al*. This article is distributed by The American Society for Cell Biology under license from the author(s). Two months after publication it is available to the public under an Attribution–Noncommercial–Share Alike 3.0 Unported Creative Commons License (http://creativecommons.org/licenses/by-nc-sa/3.0).

"ASCB®," "The American Society for Cell Biology®," and "Molecular Biology of the Cell®" are registered trademarks of The American Society of Cell Biology.

INTRODUCTION

Microtubules are highly dynamic protein filaments that play an important role in many diverse cellular processes, including cell division, architecture, migration, and intracellular transport. They are assembled from α/β-tubulin heterodimers, which align in a head-to-tail manner. Because of their intrinsic polarity, microtubules contain two structurally distinct ends: a slow-growing minus end and a fast-growing plus end (reviewed in Howard and Hyman, 2003). In cells, microtubule minus ends are often stabilized, whereas the plus ends are highly dynamic and stochastically switch between periods of growing and shortening. The intrinsically dynamic nature of microtubules is fundamental to their function, and, not surprisingly, it is strongly regulated by microtubule-associated proteins (MAPs) during cell cycle progression and cell differentiation.

Microtubule plus end–tracking proteins (+TIPs) are a specific group of MAPs that preferentially localize to the growing microtubule plus ends (Schuyler and Pellman, 2001). The end of a growing microtubule is a privileged site for +TIPs to control microtubule behavior and architecture and to link microtubules to diverse cellular structures, including kinetochores, the cell cortex, and the actin cytoskeleton (Akhmanova and Steinmetz, 2008). End-binding proteins (EBs) are evolutionarily conserved core components of +TIP interaction networks (Slep, 2010). EBs control microtubule dynamics and play a master role in targeting an array of diverse proteins to growing microtubule plus ends (Galjart, 2010). As a consequence, EBs are implicated in numerous microtubule-based cellular processes. In mammalian cells, three different members of the EB family have been described, denoted EB1, EB2 (RP1), and EB3 (EBF3) (Su and Qi, 2001).

EBs are dimeric proteins composed of two highly conserved functional modules separated by a more variable 60- to 80-residue linker region: an N-terminal calponin homology (CH) domain and a C-terminal dimerization domain (Akhmanova and Steinmetz, 2008). The CH domain mediates the interaction with microtubules (Hayashi and Ikura, 2003) and is responsible for the autonomous microtubule tip–tracking activity of EBs (Bieling *et al.*, 2007, 2008). Of interest, EBs exchange rapidly on microtubules: on the transient structure of the growing microtubule tip, which typically exists for several seconds, the residence time of EBs is less than 1 s (Bieling *et al.*, 2007, 2008; Dragestein *et al.*, 2008; Montenegro *et al.*, 2010). It is unknown which features of the growing microtubule plus end are specifically recognized by the CH domains of EBs. Three hypotheses have been proposed. First, EBs may recognize the open and extended tubulin sheet structure at microtubule tips (Vitre *et al.*, 2008). Second, EBs might preferentially bind to or impose a structural discontinuity—for example, A versus B lattice—at the plus end of a growing microtubule (Sandblad *et al.*, 2006; des Georges *et al.*, 2008). Finally, a third model suggests that EBs sense the guanine nucleotide state of β-tubulin to discriminate between GTP-tubulin at the growing tip and GDP-tubulin in the lattice (Zanic *et al.*, 2009; Maurer *et al.*, 2011).

The C-terminal domain of the EBs comprises a coiled coil, the unique EB-homology (EBH) domain, and a disordered 20- to 30-residue tail (Honnappa *et al.*, 2005; Slep *et al.*, 2005). The EBH domain and the tail region are responsible for parallel homodimerization and heterodimerization of EB subunits and for partner binding (Honnappa *et al.*, 2009; De Groot *et al.*, 2010). Dimer formation enhances the affinity of some EB family members for microtubules, and in some cases is even essential for microtubule tip binding (Slep and Vale, 2007; Komarova *et al.*, 2009; Zimniak *et al.*, 2009). The CH domain and the linker region comprise positively charged sequence regions, which contribute to the binding to the negatively charged microtubule lattice (Hayashi and Ikura, 2003; Slep and Vale, 2007; des Georges *et al.*, 2008). In contrast, the C-terminal part of EBs is negatively charged due to acidic residues present on the surface of the EBH domain and in the disordered C-terminal tail region (Honnappa *et al.*, 2005; Slep *et al.*, 2005).

How the CH and C-terminal domains are organized in the context of the full-length EB molecule, how they control its partner-binding activity, and how they enable EBs to specifically recognize the plus end of a growing microtubule is only poorly understood. On the basis of the crystal structures of isolated CH and C-terminal domains of EB1 and the lack of regular secondary structure predicted for the linker region, one could expect that the two CH domains of EB1 are independent and freely diffusible (Honnappa *et al.*, 2005). Biochemical studies have suggested that the C-terminal acidic tail of EB1 regulates its microtubule-binding and tubulin polymerization activity (Hayashi *et al.*, 2005; Manna *et al.*, 2008; Zhu *et al.*, 2009). To explain this observation, it has been proposed that EB1 exists in a "closed," autoinhibited conformation formed by a head-to-tail interaction between the acidic tail and the basic CH domain (Hayashi *et al.*, 2005). In this model, removal of the acidic tail or binding of partners to the C-terminal domain relieves this autoinhibited state by opening up the molecule into an activated conformation, which enables tighter binding of EB1 to microtubules and, as a consequence, enhances tubulin polymerization (Hayashi *et al.*, 2005). In contrast to these in vitro observations, studies in cells showed that although the removal of the acidic tail of EBs blocked partner binding (Komarova *et al.*, 2005), it had little effect on their microtubule tip accumulation and their capacity to suppress catastrophes (Komarova *et al.*, 2009).

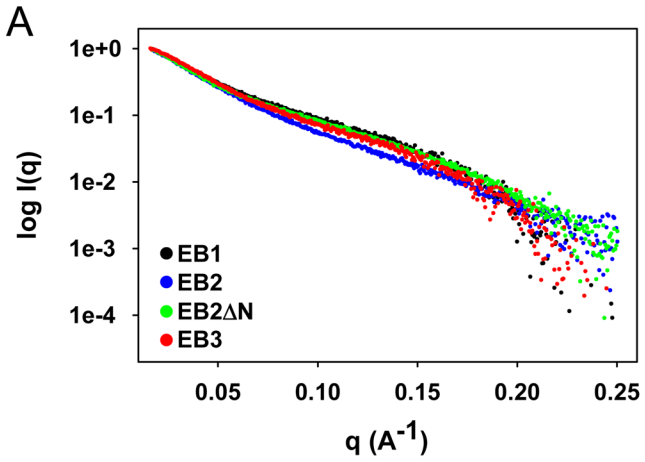
We used a combination of structural, biophysical, and biochemical methods to analyze the conformation of full-length human EBs and to assess how the C-terminal domain of EBs controls their microtubule-binding activity. We show that EB1, EB2, and EB3 display a similar conformation in solution, characterized by an elongated shape, and provide data supporting a model in which the two CH domains within EB dimers can interact with each other. Removal of the C-terminal tail of EB1 did not affect the global conformation of the protein, a result that does not support the aforementioned closed-to-open activation model. However, in vitro microtubule tip–tracking experiments suggest that the negatively charged nature of the entire C-terminal domain of EB promotes the specificity of the molecule for the growing microtubule plus ends as opposed to the microtubule lattice. In combination, our data provide new insights into the structure of the EBs and the mechanism of their specific localization at the microtubule tip.

RESULTS

Solution small-angle x-ray scattering analysis of human EBs

To gain insight into the structures of EBs, we performed small-angle x-ray scattering (SAXS) experiments with human EB1, EB2, and EB3 homodimers. Figure 1A shows the SAXS profiles of the three proteins, which are all very similar (see Supplemental Figure S1 for raw data). Accordingly, the calculated radius of gyration, R_g, and maximum particle distance, D_{max}, were found to be alike, amounting to 46.8 and 140 Å, 47.1 and 141 Å, and 45.2 and 136 Å for EB1, EB2, and EB3, respectively (Figure 1B).

The similar pair distribution functions (PDFs), which represent histograms of interatomic distances of EB1 and EB3, are characterized by the presence of two main peaks centered at around 24 and 46 Å (Figure 1C). Comparison of these peaks with the single one obtained for the isolated CH domain of EB1 suggests that the first peak mainly represents interatomic distances within this module,



B

	EB1	EB1ΔTail	EB2	EB2ΔN	EB3
$R_{g\ Guinier}$ (Å)	46.8 ± 0.5	45.2 ± 1.5	47.1 ± 0.3	50.6 ± 0.3	45.2 ± 0.1
$R_{g\ PDF}$ (Å)	46.1 ± 1.6	44.4 ± 2.3	47.7 ± 2.7	50.0 ± 2.7	45.1 ± 1.4
D_{max} (Å)	140	136	141	152	136

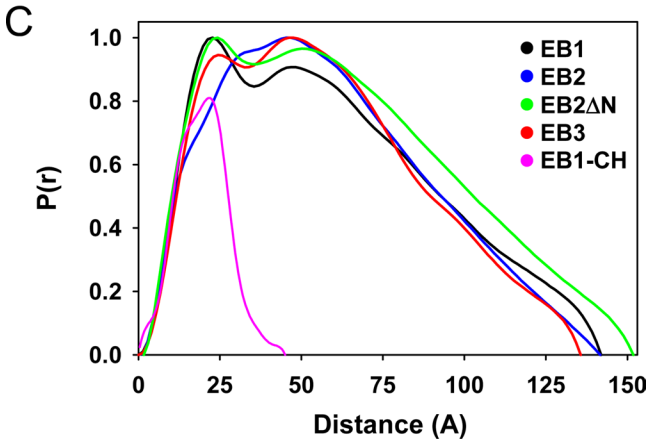


FIGURE 1: SAXS analysis of EBs. (A) Experimental SAXS scattering profiles of EB1 (black), EB2 (blue), EB2ΔN (green), and EB3 (red). (B) R_g (calculated from Guinier plot and PDFs) and D_{max} values of EB1, EB2, and EB3. (C) PDFs calculated with AutoGNOM of EB1, EB2, EB2ΔN, EB3, and EB1-CH. Colors are the same as in A; EB1-CH is in pink.

whereas the second peak corresponds to longer distances between the CH and C-terminal domains (Figure 1C). Notably, for EB2 the first peak is displaced by ~8 Å to longer distances. EB2 contains a 43-residue-long N-terminal extension not present in EB1 and EB3, which is predicted to fold into two short β-strands (Supplemental Figure S2). Deletion of this N-terminal extension in EB2 (EB2ΔN) resulted in a SAXS profile and PDF that are similar to the ones obtained for EB1 and EB3 (Figure 1, A and C). Therefore, the displacement observed for the first peak can be attributed to the N-terminal extension of EB2, which increases the size of its N-terminal domain. The fact that EB2 has a slightly smaller R_g than EB2ΔN (Figure 1B) indicates that the N-terminal extension restricts the conformational space of the full-length protein in solution. The functional relevance of the N-terminal EB2 extension is not clear; experiments in cells indicated that it does not influence the ability of EBs to accumulate at microtubule tips and suppress catastrophes (Komarova *et al.*, 2009).

Together, these data demonstrate that the overall dimensions and spatial arrangement of the CH, linker, and C-terminal domains are similar for the three human EBs, consistent with their overall high sequence identity (Su and Qi, 2001).

Structural model of EBs

To obtain the low-resolution structure of an EB protein, we performed ab initio modeling using the SAXS data just described. Two different modeling methods based on genetic and simulated annealing algorithms were used (see *Materials and Methods*). Both approaches generated models that are very similar in their overall conformation and were consistent within the resolution limits of SAXS (Supplemental Figures S3 and S4 and Supplemental Tables S1–S3). The consensus model depicts EB as an elongated and globally asymmetric molecule, which recalls a golf club (Figure 2A). The calculated sedimentation coefficient for the model is 3.22 S, in good agreement with the experimental value of 3.15 S derived by analytical ultracentrifugation (Honnappa *et al.*, 2005), supporting the reliability of our model.

The low-resolution SAXS envelope reveals two main structural features: a rod-like structure ~9 nm in length and two globular domains that interact with each other, forming a ~8-nm, dumbbell-shaped structure. The dimensions and shapes of these structural features can be assigned to the C-terminal and CH domains of EB, respectively, whose x-ray structures were manually docked into the molecular envelope (Figure 2A). However, we note that this docking is not unambiguous but is one reasonable possibility to interpret the low-resolution SAXS envelope. Despite EBs being homodimers, we did not find any evidence for a global symmetry in the SAXS data (see *Materials and Methods*). The close proximity of the CH and C-terminal domains in the SAXS envelope suggests that parts of the 60-residue-long linker regions are folded to some extent and could be involved in organizing an interacting pair of CH domains in a way that does not maintain the overall twofold symmetry of the coiled coil. An asymmetric arrangement of interacting homotypic domains has been observed in, for example, activated epidermal growth factor (EGF) receptor (EGFR). Similar to the CH domains of EBs, the asymmetrically interacting kinase domains of the EGFR homodimer are separated by a polypeptide linker from their transmembrane domain, which displays a twofold symmetry (Jura *et al.*, 2009).

Next we used electron microscopy to directly visualize the conformation of EBs. Because of the similar overall size of the CH and C-terminal domains, it was not possible to unambiguously distinguish them previously in rotary metal-shadowed EB1 specimens (Honnappa *et al.*, 2005). To overcome this problem, we fused the CH-linker moiety of EB1 in tandem to the parallel two-stranded coiled coils of GCN4 and cortexillin-1 (EB1-NL-LZ-Cort). We previously showed that the EB3-NL-LZ chimera (CH-linker of EB3 fused to GCN4) was functional and able to track microtubule ends (Komarova *et al.*, 2009), validating the approach. Electron micrographs of rotary metal-shadowed EB1-NL-LZ-Cort revealed rod-like specimens that displayed a single head-like moiety at one extremity (Figure 2B). The 24- to 26-nm size of the rod agrees well with the predicted length of the GCN4–cortexillin coiled-coil fusion (24 nm). Accordingly, the head moiety corresponds to the CH domains; its size (8–13 nm) fits the size of the pair of interacting CH domains in our SAXS-based EB model (Figure 2A). We note that the appearance of the head moiety is heterogeneous, which is most likely due to the different views of the specimens on the electron microscopy grid and to some flexibility at the interface junction of the head and coiled-coil domain. To obtain a better signal-to-noise ratio, we performed image analysis and classification. As shown in Figure 2C, averaged images of the head domain of EB1-NL-LZ-Cort revealed

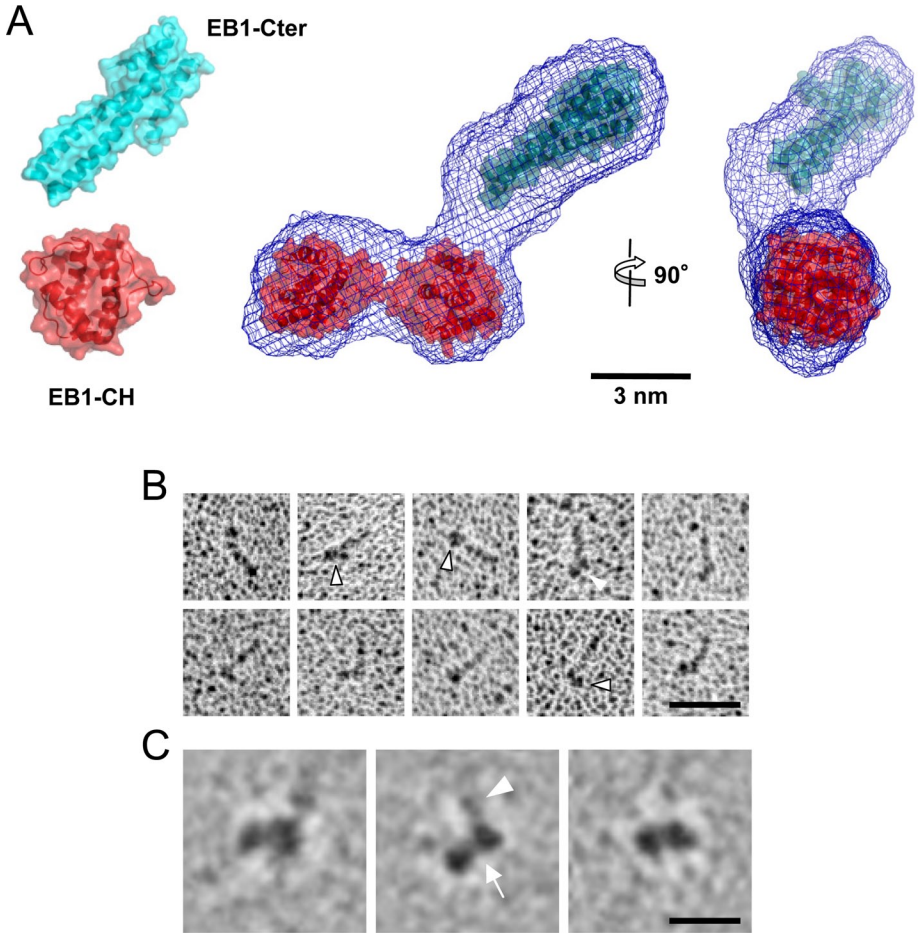


FIGURE 2: EB model. (A) Calculated SAXS envelope (blue mesh) of EB1. The crystal structures of the CH (red ribbon; PDB ID 1PA7) and C-terminal domains (blue ribbon; PDB ID 1WU9) of EB1 are manually docked into the map. (B) Electron micrographs of rotary metal-shadowed EB1-NL-LZ-Cort specimens. The head moiety corresponding to the CH domains is highlighted by an arrowhead. Scale bar, 50 nm. (C) Averaged images of the head domain of EB1-NL-LZ-Cort specimens shown in B. Arrow and arrowhead (middle) highlight the CH and coiled-coil domains, respectively. Scale bar, 10 nm.

two connected globular particles corresponding to the CH domains. A part of the coiled-coil rod domain is visible in some cases (Figure 2C, left and middle) but is occasionally smeared out, probably due to some intrinsic flexibility (Figure 2C, right). The averaged images are strikingly similar to the molecular envelope obtained with EB1 by SAXS in solution (Figure 2A).

To obtain conformational restraints on intradimer protein contacts at the single-residue level, we carried out chemical cross-linking experiments with the EB1 and EB3 homodimers and with the EB1–EB3 heterodimer (Supplemental Figure S5A; De Groot *et al.*, 2010) and identified cross-linked tryptic peptides by mass spectrometry (MS). Disuccinimidyl suberate (DSS) was used as cross-linker. DSS mainly reacts with primary amines and connects lysine side chains of proteins that are within a maximum distance of 25 Å (measured from Cα backbone atoms) (Seebacher *et al.*, 2006; Leitner *et al.*, 2010). The mass spectral analysis and subsequent identification of cross-linked residues revealed a total of 123 unique and unambiguously assignable cross-linked peptides (Supplemental Figure S5B and Supplemental Table S4). From those, 47 cross-linked residues were identified unambiguously as intermolecular cross-links (i.e., CH–CH, CH–linker, linker–linker, linker–C-terminal domain; Figure 3A). The high number and the characteristic arrangement of these cross-links are indicative of a large dimer interface and suggest that the linker region can reach both the CH and C-terminal domains.

Three interprotein cross-links that involved residues between the CH domains were identified (Supplemental Figure S6): EB1-K113:EB1-K113, EB1-K113:EB1-K122, and EB1-K95:EB3-K122. These were used as distance constraints to orient the two CH domains seen in our SAXS and electron microscopy data with respect to each other. Although the modeling is not unambiguous concerning the details, we were able to manually generate a plausible model in which the residues known to be important for microtubule binding (Slep and Vale, 2007) cluster into two distinct patches on the dimeric CH–CH surface (Figure 3B). Notably, the spatial arrangement of these two patches would be accessible for microtubule binding in a manner compatible with the previously proposed interprotofilament interaction model (Sandblad *et al.*, 2006; des Georges *et al.*, 2008).

These data suggest that EBs are elongated dimeric molecules. Collectively, they further consistently support the model that the two CH domains within the EB dimer interact and can potentially form a composite microtubule-binding interface.

The C-terminal tail does not affect the global conformation of EBs

It has been proposed previously that EB1 exists in an autoinhibited conformation, which is formed by a head-to-tail interaction between the CH domain and the 20-residue-long C-terminal acidic tail (Hayashi *et al.*, 2005). The model predicts that on removal of the acidic tail or binding of partners to the C-terminal domain, EB1 is activated by undergoing a large change from a "closed" to an "open" conformation. To test this model, we analyzed by SAXS an EB1 mutant in which the tail region was deleted (EB1ΔTail). The shape of the scattering profile and accordingly the calculated R_g and D_{max} values for EB1ΔTail were found to be very similar to those of the full-length protein (Figures 1B and 4, A and B, and Supplemental Figures S1B and S3B). A similar result was obtained for EB3 and EB3ΔTail (Supplemental Figures S1C and S3C). These findings demonstrate that the presence of the acidic tail has no strong effect on the global conformation of EBs.

The C-terminal domain promotes dissociation of EBs from the microtubule lattice

If the acidic tail does not activate the EBs by controlling their overall conformation (see earlier discussion), what is its role for the microtubule-directed activities of EBs? To address this question, we used an in vitro microtubule plus end–tracking assay (Bieling *et al.*, 2007), which allows examination of the intrinsic ability of EB proteins to interact with dynamic microtubule tips and with the microtubule lattice. For these experiments, we used EB3 because, in contrast to EB1, the plus end–tracking behavior of

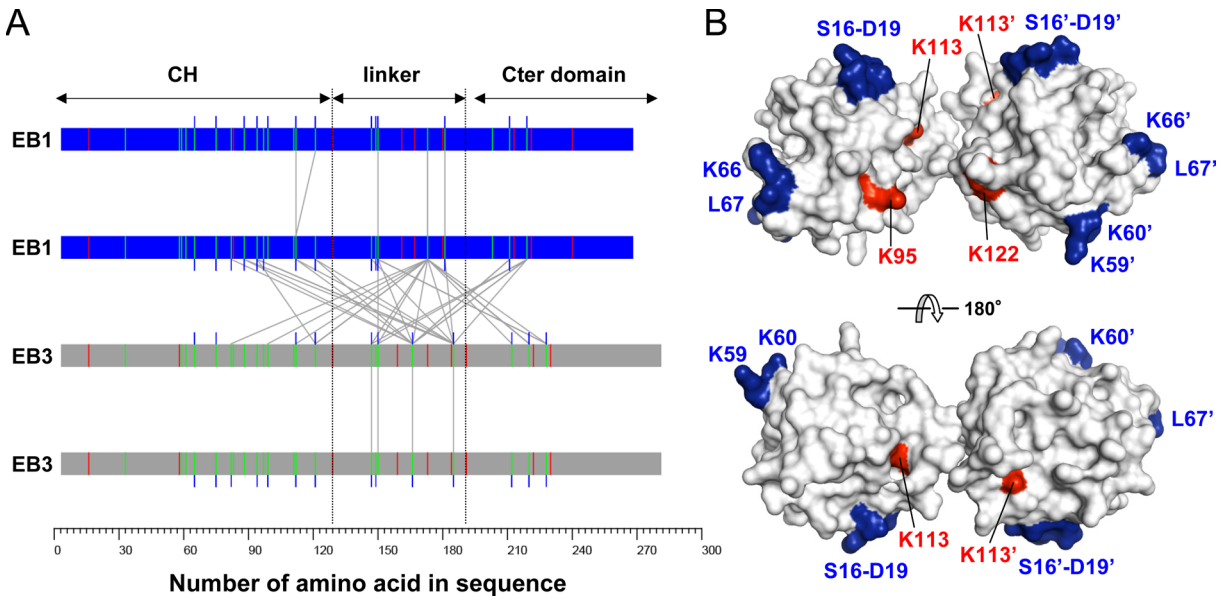


FIGURE 3: Chemical cross-linking of EBs. (A) Intermolecular map of identified cross-links between lysine residues of EB1–EB1, EB1–EB3, and EB3–EB3 dimers. The proteins are depicted as bars, and cross-linked lysines (green vertical lines) are indicated by gray lines. Monolinks (blue vertical lines) and tryptic cleavage sites (arginine; red vertical lines) are marked. (B) Model of the CH domain pair. Red and blue residues were found to be cross-linked by DSS and to interact with microtubules (Slep and Vale, 2007), respectively.

EB3 tolerates the addition of an N-terminal green fluorescent protein (GFP) tag (Komarova *et al.*, 2009; Montenegro *et al.*, 2010; Skube *et al.*, 2010). This property is a prerequisite for experiments aimed at investigating the function of the C-terminal tail of EB. In addition to EB3 and EB3ΔTail, we also included in our experiments an EB3 variant in which the entire C-terminal domain was replaced by the parallel, two-stranded coiled-coil domain of GCN4 (EB3-NL-LZ) (Figure 5A). In contrast to the overall acidic C-terminal domain (Honnappa *et al.*, 2009), the GCN4 coiled coil is neutral (O'Shea *et al.*, 1991). As a consequence, the EB3-NL-LZ chimera is much more positively charged than wild-type EB3 (Figure 5A). Note that we previously showed in cells that EB3-NL-LZ accumulates at growing microtubule tips and can substitute for endogenous EB1 and EB3 in suppressing microtubule catastrophes (Komarova *et al.*, 2009).

At 10 nM concentration, all three proteins preferentially decorated growing microtubule tips and only weakly bound along the microtubule lattice (Figure 5, B and C, and Supplemental Figure S7A). Quantification of the fluorescence intensities showed that the accumulation of the three proteins at growing microtubule plus ends was similar (Table 1). However, EB3ΔTail showed enhanced lattice binding and therefore a lower tip-to-lattice intensity ratio (Figure 5D). This effect was even more pronounced for EB3-NL-LZ (Figure 5D), which also consistently displayed a weak but clearly detectable accumulation at depolymerizing microtubule ends (Figure 5C, arrows). Such an accumulation was never observed for the full-length EB3 but was occasionally seen with EB3ΔTail (Figure 5C, arrows). On the basis of these findings, we hypothesize that the microtubule lattice interaction of EB3 is suppressed by long-range nonspecific electrostatic repulsion between the negatively charged outer surface of

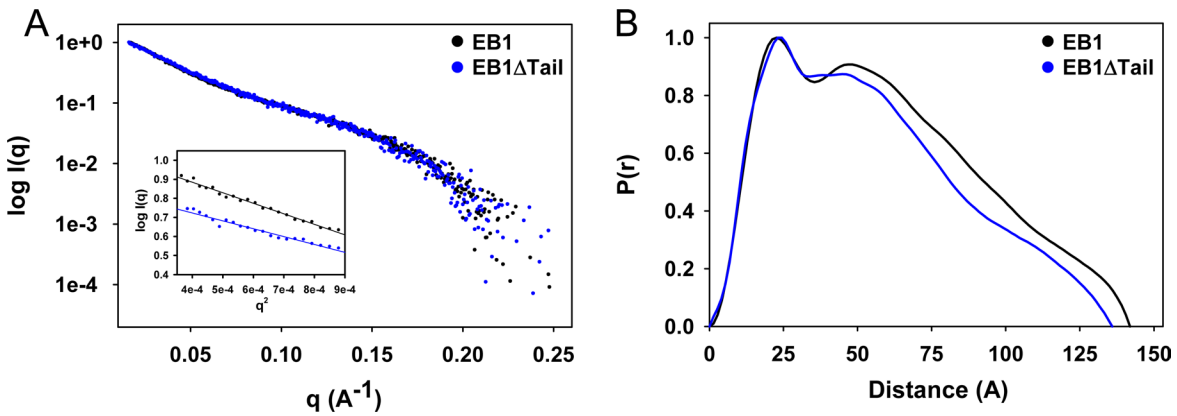
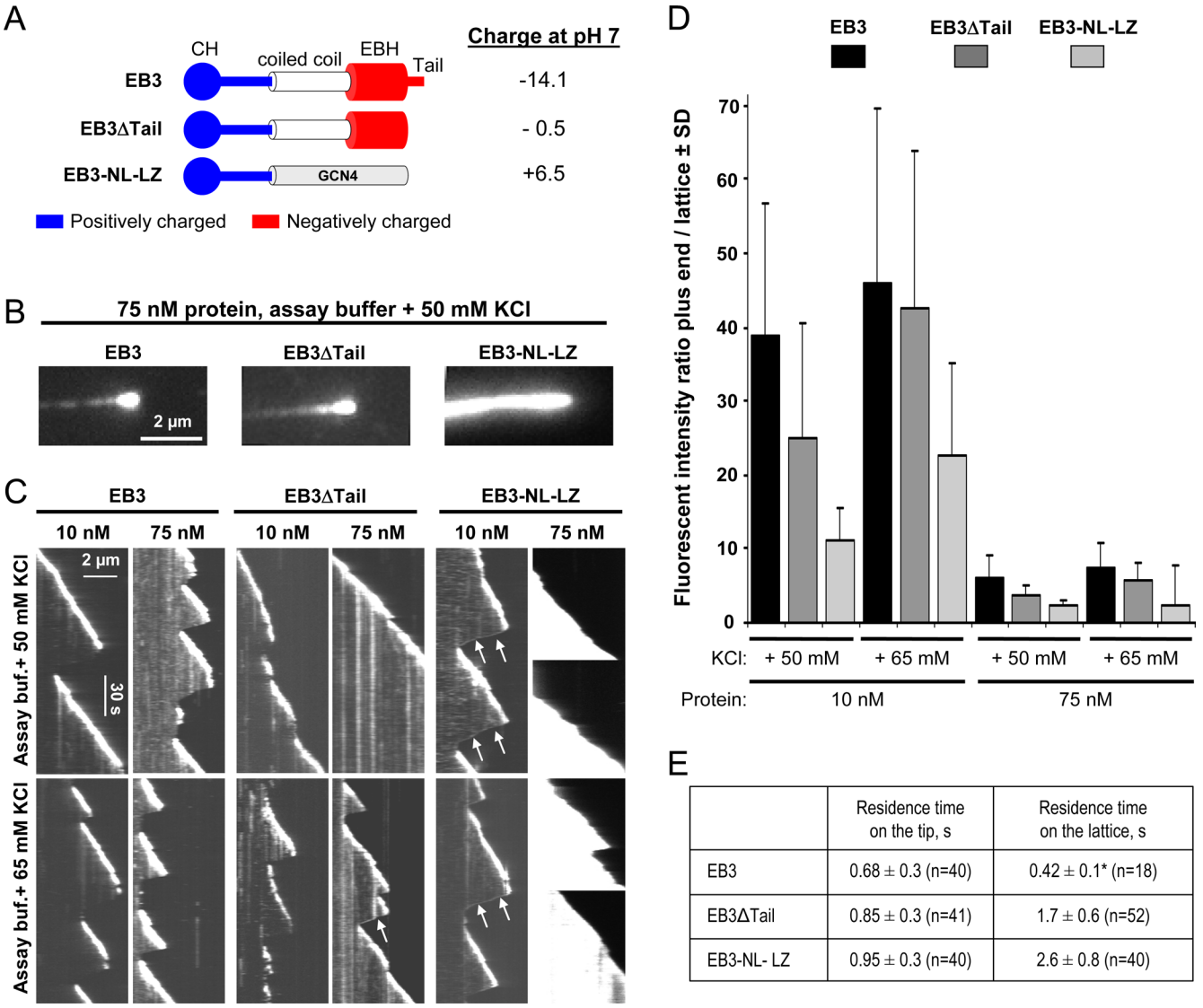


FIGURE 4: Role of the acidic tail for EB structure. (A) SAXS profiles and (B) PDFs of EB1 (black) and EB1ΔTail (blue). Inset in A, Guinier plots.



	Residence time on the tip, s	Residence time on the lattice, s
EB3	0.68 ± 0.3 (n=40)	0.42 ± 0.1* (n=18)
EB3ΔTail	0.85 ± 0.3 (n=41)	1.7 ± 0.6 (n=52)
EB3-NL- LZ	0.95 ± 0.3 (n=40)	2.6 ± 0.8 (n=40)

FIGURE 5: Role of the C-terminal domain in the specific enrichment of EBs at growing microtubule ends. (A) GFP-EB3 variants used in the in vitro plus end–tracking assay. The positively and negatively charged nature of the CH and C-terminal domains is indicated by blue and red, respectively. The net charge of the different GFP-tagged EB3 variants at pH 7 (based on the theoretical pI of the sequence) is indicated on the right. (B) TIRFM images and (C) kymographs of dynamic microtubules grown in the presence of the indicated concentrations of GFP-tagged EB3 protein variants. The concentration of KCl added to the buffer is also stated. Accumulation of GFP-tagged EB3-NL-LZ at the depolymerizing microtubule ends is marked by arrows. (D) Plots indicating fluorescence intensity ratios of growing microtubule ends vs. microtubule lattice for GFP-tagged EB3, EB3Δtail, and EB3-NL-LZ at different protein and salt concentrations (indicated below the plots). All measurements were performed with the same laser intensity, with the exception of 75 nM EB3-NL-LZ, for which the laser power was reduced to avoid signal saturation. (E) In vitro residence time of EB3 and its mutants on microtubule tips and lattice, measured by FRAP. All measurements were performed at 75 nM protein, with the exception of the residence time of full-length EB3 on the lattice (*), which was measured at 300 nM EB3 to obtain a sufficiently high signal to perform meaningful measurements.

the microtubule lattice (Baker *et al.*, 2001) and the negatively charged C-terminal portion of the protein. This repulsion seems to counteract the electrostatic attractive interaction between the negatively charged microtubule lattice and the positively charged CH-linker domain of EB3 (des Georges *et al.*, 2008; Komarova *et al.*, 2009).

To test whether the binding of EB3 to the microtubule lattice is driven by electrostatic interactions, we increased the concentration of KCl added to the buffer from 50 to 65 mM. Addition of higher amounts of salt was not possible due to a dramatic increase in microtubule catastrophe frequency and the ensuing inhibition of microtubule growth. Consistent with previous findings (Zanic *et al.*, 2009), we found that although the 30% increase in the concentration of the added salt had little effect on the accumulation of the three EB3 variants (10 nM) at microtubule tips, it reduced their accumulation on the microtubule lattice and, as a consequence, caused an increase in the tip-to-lattice intensity ratio (Figure 5D and Table 1). The reduction in microtubule lattice binding at increased salt concentration was most pronounced for EB3-NL-LZ.

	10 nM protein						75 nM protein					
	+ 50 mM KCl			+ 65 mM KCl			+ 50 mM KCl			+ 65 mM KCl		
	Tip/ lattice	Intensity, AU ×10^3	N	Tip/ lattice	Intensity, AU ×10^3	N	Tip/ lattice	Intensity, AU ×10^3	N	Tip/ lattice	Intensity, AU ×10^3	N
EB3	38.9 ± 17.8	42.4 ± 6.8	105	45.9 ± 23.5	40.2 ± 5.2	126	6.2 ± 2.9	42.8 ± 11.1	143	7.5 ± 3.2	52.7 ± 5.6	115
EB3 ΔTail	24.9 ± 15.5	34.3 ± 10.1	147	42.7 ± 21.1	45.6 ± 8.1	71	3.7 ± 1.4	42.4 ± 7.2	121	5.6 ± 2.6	49.6 ± 10.2	102
EB3-NL-LZ	11.0 ± 4.6	47.6 ± 4.0	101	22.7 ± 12.4	38.3 ± 5.6	111	2.3 ± 0.8	45.5 ± 5.7[a]	26	2.4 ± 5.2	37.2 ± 6.1[a]	28

Microtubule plus end–tracking in vitro experiments were performed for EB3, EB3Δtail, and EB3-NL-LZ at different protein and salt concentrations, as indicated. Documented are the average tip-to-lattice fluorescence intensity ratio (± SD), average fluorescence intensity (AU, arbitrary units) at microtubule growing ends (± SD), and number of measured microtubule tips (N) for each condition. Measurements were performed using kymographs as described in *Materials and Methods*.
[a]The intensity values for 75 nM EB3-NL-LZ cannot be compared with the other intensity values because the laser power was reduced to avoid signal saturation. The tip-to-lattice ratios were always measured within the same image and thus can be compared between all experiments.

TABLE 1: Fluorescence intensities at microtubule ends and fluorescence intensity ratios between growing microtubule ends and microtubule lattice in different conditions.

Next we performed similar experiments using 75 nM EB3 proteins. The 7.5-fold increase in protein concentration compared with the previous experiments had little effect on the intensity of GFP signal of EB3 and EB3ΔTail at microtubule tips (Supplemental Figure S7A and Table 1), indicating that the binding sites at microtubule tips are already saturated at 10 nM EB3 or EB3ΔTail. However, the microtubule lattice signal was strongly increased for EB3 and EB3ΔTail, resulting in a significant reduction of the tip-to-lattice ratio. This result is in agreement with observations in cells, where EBs preferentially associate with microtubule tips at endogenous protein levels but decorate the whole microtubule cytoskeleton when overexpressed (Ligon *et al.*, 2003).

For EB3-NL-LZ the enhancement of lattice binding at 75 nM protein concentration was so pronounced that in ~80–90% of all cases growing tips could not even be distinguished from the rest of the microtubule bodies (Figure 5, C and D, and Supplemental Figure S7B). Still, on some microtubules, EB3-NL-LZ was brighter at the tip than at the adjacent lattice (Figure 5C and Supplemental Figure S7B). Such irregularities in microtubule lattice decoration by EB3-NL-LZ might point to its ability to locally change microtubule lattice properties—for example, promote the formation of A lattice as described for Mal3 (des Georges *et al.*, 2008). Local microtubule lattice deviations or defects might also account for the presence of sites with an enhanced and stable EB3 association, which appeared as vertical lines in kymographs and were more prominent for EB3ΔTail than for full-length EB3 (Figure 5C).

The increased accumulation of EB3 mutants lacking the tail or the whole C-terminal domain might be due to their reduced dissociation from the microtubule lattice. To test this idea, we measured the turnover of EB3 and its mutants on microtubule tips and lattices by fluorescence recovery after photobleaching (FRAP) analyses. For the full-length EB3, the residence time on the tip was longer than that on the lattice, in agreement with our previous observations based on single-molecule imaging (Figure 5E; Montenegro *et al.*, 2010). We note that the residence-time values obtained by FRAP were higher than those obtained by observing single GFP-EB3 molecules. This was possibly due to the different analytical procedures used in the two types of experiments or because our FRAP experiments were performed at ~200–1000 times higher concentration of GFP-EB3, which might behave differently in these conditions. Of interest, the residence time of both C-terminal mutants, EB3ΔTail and EB3-NL-LZ, on the microtubule lattice was significantly longer than that of native EB3, in line with the view that the negatively charged C-terminal domain promotes EB dissociation from the microtubule lattice. This effect was less pronounced at the growing microtubule tip, supporting the idea that the EB-binding sites at the microtubule tip and lattice exhibit distinct properties.

Effects of the C-terminal domain of EBs on microtubule dynamics and assembly

The differences among the three EB3 proteins in their microtubule interaction properties are also reflected in their effects on microtubule dynamics in vitro. We previously showed that full-length EB3 causes an increase in microtubule growth rate but also promotes catastrophes (Komarova *et al.*, 2009). Of interest, the catastrophe-promoting activity of EB3ΔTail at 75 nM concentration was lower than that of the full-length protein (Montenegro *et al.*, 2010). In the presence of 75 nM EB3-NL-LZ, no catastrophes were observed, making it impossible to measure microtubule depolymerization rates and transition frequencies in these conditions. Therefore, the enhanced capacity of the C-terminal mutants of EB3 to decorate the microtubule lattice correlates with a reduced catastrophe-promoting activity. In the presence of 10 nM EB3 or its mutants, when only microtubule tips but not the lattices were strongly decorated, the parameters of microtubule dynamics were very similar for all three proteins tested (Supplemental Table S5). However, an enhanced tendency for promoting rescues was observed for EB3-NL-LZ, in agreement with its higher accumulation on the microtubule lattice (Supplemental Table S5 and Figure 5, C and D).

To further investigate the role of the C-terminal domain for EB activity, we analyzed its effect on microtubule assembly in vitro in a bulk assay at high EB concentration. For these experiments, which do not require the use of fluorescent fusions, we used EB1 to enable direct comparison with previously published data. We first compared the kinetics of tubulin polymerization in the presence of EB1 or EB1ΔTail using an assay based on measurement of 4′,6-diamidino-2-phenylindol (DAPI) fluorescence (Bonne *et al.*, 1985). Under these experimental conditions, we could detect very little polymerization of 25 μM tubulin within the 70-min time frame of the experiment, and the addition of 12.5 μM EB1 had no effect on tubulin polymerization (Figure 6). In contrast, in the presence of EB1ΔTail, microtubules started to assemble after a lag phase, in agreement with previous observations showing that the acidic tail negatively regulates binding to microtubules and, as a consequence, the tubulin polymerization activity of EB1 (Hayashi *et al.*, 2005; Manna *et al.*, 2008; Zhu *et al.*, 2009). Notably, the increased capacity of EB1ΔTail to promote tubulin polymerization correlated with the concentration dependence of enhanced microtubule lattice binding observed

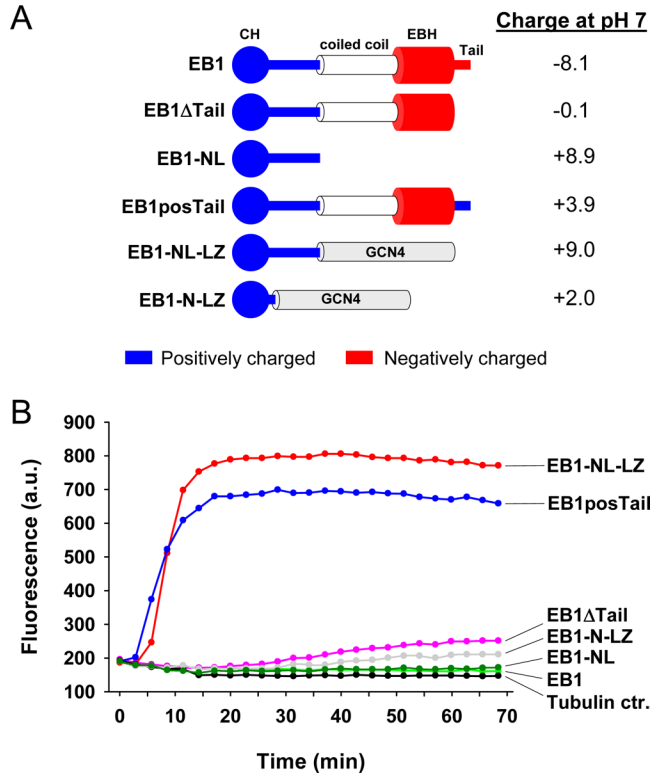


FIGURE 6: Role of the C-terminal domain of EB1 on tubulin polymerization. (A) EB1 constructs used for the tubulin polymerization experiments. The positively and negatively charged nature of the CH and C-terminal domains is indicated by blue and red, respectively. The net charge of the different EB1 variants at pH 7 (based on the theoretical pI of the sequence) is indicated on the right. (B) Tubulin polymerization followed by DAPI fluorescence in the absence (black) and presence of EB1 (light green), EB1-NL (dark green), EB1-N-LZ (gray), EB1ΔTail (pink), EB1posTail (blue), and EB1-NL-LZ (red).

for the ΔTail mutant of EB3 (Figure 5, C and D). A superior microtubule lattice binding and the subsequent increase in tubulin polymer mass was qualitatively confirmed by label-free microtubule pelleting experiments in the presence of EB1 or EB1ΔTail (Supplemental Figure S8).

Because EB3-NL-LZ bound very strongly along microtubules at high concentration (Figure 5, C and D; see also Supplemental Figure S8 for comparison of EB1 vs. EB1-NL-LZ), we expected that a similar EB1 variant would exhibit a very pronounced effect on promoting tubulin polymerization, and we found that this was indeed the case (Figure 6 and Supplemental Figure S8). A similar effect was observed using an EB1 mutant in which the eight acidic residues of the C-terminal tail were simultaneously replaced by basic lysines (EB1posTail). In contrast, a shorter version of EB1-NL-LZ in which the linker region between the CH and EBH domains was shortened to six residues (EB1-N-LZ) was not able to efficiently induce tubulin polymerization; its activity was comparable to a monomeric EB1 fragment encompassing only the CH domain plus linker region (EB1-NL; Figure 6 and Supplemental Figure S8).

In combination, our microtubule tip tracking and tubulin polymerization data suggest that the global negatively charged nature of the C-terminal domain suppresses the electrostatic interaction of the EBs with the negatively charged outer surface of the microtubule lattice, therefore promoting specificity for the growing microtubule plus end. They further indicate that a dimeric arrangement including a complete linker is necessary for creating a fully active EB molecule.

DISCUSSION

In this study we sought to investigate the structure and mechanism of microtubule tip binding of mammalian EBs. Our SAXS, electron microscopy, and chemical cross-linking data suggest a coherent structural model of EB in which the protein adopts an elongated conformation with two interacting CH domains. The linker region appears folded to some extent and interacts with both the CH and C-terminal domains to form a complex interaction interface. The C-terminal dimerization domain is necessary to stabilize this arrangement, since no dimers are observed for the isolated CH-linker fragments (Sandblad *et al.*, 2006; des Georges *et al.*, 2008; Komarova *et al.*, 2009; unpublished data).

We recently reported that a construct encompassing the CH-linker region of EB3 is sufficient for microtubule tip tracking (Komarova *et al.*, 2009). However, compared with dimeric full-length EB3, this monomeric construct displayed strongly reduced microtubule tip localization and was unable to promote processive microtubule growth in cells. Consistent with an important role of dimerization, the analogous CH-linker constructs of *Drosophila melanogaster* EB1 and the one of the yeast EB orthologue Bim1p failed to show any microtubule tip–tracking activity (Slep and Vale, 2007; Zimniak *et al.*, 2009). In this context, a microtubule-binding interface composed of a pair of interacting CH domains offers an attractive model for explaining why an intact EB molecule is needed for robust tracking of growing microtubule plus ends and for controlling processive microtubule growth in cells. Moreover, our tubulin polymerization data further support the notion that the linker region contributes to microtubule affinity of the EBs (des Georges *et al.*, 2008; Komarova *et al.*, 2009).

F-Actin–binding CH domains frequently occur as interacting pairs (Gimona *et al.*, 2002). Of interest, a pair of interacting CH domains that form a composite microtubule-binding interface was recently reported for the kinetochore Ndc80/Nuf2 complex (Ciferri *et al.*, 2008), whose overall shape strikingly recalls that of our low-resolution EB model (Supplemental Figure S9, A and B). Similar to EBs, the two microtubule-binding, N-terminal CH domains of the Ndc80/Nuf2 complex are followed by a linker region and a coiled-coil dimerization domain (Supplemental Figure S9C). Furthermore, the same sequential arrangement of CH–linker–coiled coil is also found for the microtubule-binding protein Spef1/CLAMP (Supplemental Figure S9C; Dougherty *et al.*, 2005). On the basis of these considerations, we hypothesize that interacting pairs of CH domains may represent a general property of microtubule-binding CH domains. Because of the very low degree of sequence conservation between the CH domains and linker regions of EBs, Ndc80, Nuf2, and Spef1/CLAMP (<15% sequence identity), we expect that the orientation of the interacting CH domains with respect to each other are very likely different between these proteins. Consistent with this conclusion is the observation that in contrast to the EBs, both the Ndc80/Nuf2 complex and Spef1/CLAMP do not track growing microtubule plus ends. It is important to stress that although our hypothesis of interacting pairs of CH domains in microtubule-binding proteins seems plausible and attractive, our data could also be interpreted in the context of alternative models due to current experimental limitations. In particular, we do not know whether the two CH domains remain bound to each other once the EB molecule interacts with a growing microtubule tip. More work is required to investigate this important question further.

Our SAXS data on EBs and EBΔTail demonstrate that removal of the C-terminal acidic tail does not significantly affect the global EB structure. This result does not provide support to the EB activation model suggesting a large change from a "closed" to an "open" conformation, which is supposed to be controlled by the tail region (Hayashi *et al.*, 2005). However, our biochemical and microscopy data suggest that the primary role of the acidic tail, and in fact of the entire acidic C-terminal EB domain, is to suppress binding of EBs to the microtubule lattice but not to the growing microtubule tip, most probably by long-range nonspecific electrostatic repulsion (see also later discussion). Our data therefore provide an alternative and plausible explanation for the effect of the acidic tail on the EB1-induced tubulin assembly observed in vitro.

The monomeric EB3-NL fragment has a much lower affinity for microtubule tips compared to dimeric EB3 versions (Komarova *et al.* 2009). In line with this observation, we found that EB1-NL did not significantly promote microtubule polymerization even when added at a very high concentration. In cells, EB3-NL weakly decorates microtubule tips in the absence of endogenous EB1 and EB3 but shows no significant decoration of the microtubule lattice, which is in contrast to, for example, the artificial EB3-NL-LZ dimer (Komarova *et al.* 2009; unpublished data). Dimerization of the CH domains with the adjacent linker regions thus makes the interaction with microtubules more robust. This stabilizing effect, however, goes at the expense of specificity: at elevated concentrations, EB3-NL-LZ dimers bind not only to microtubule ends, but also along the microtubule lattice. Electrostatic repulsion between the negatively charged C-terminal domain of EBs and the microtubule lattice is thus used to overcome this loss in specificity in dimeric native EB proteins.

The yeast EB homologue Mal3 was shown to have a 10-times-higher affinity for the growing tip than for the stable lattice (Maurer *et al.*, 2011), suggesting that the interaction mechanism for the microtubule lattice versus the tip is different. Our microtubule tip–tracking, tubulin polymerization, and microtubule-binding data support this view. First, we also find that the affinity for the microtubule tip is much greater than that for the lattice. This is demonstrated by the fact that already at 10 nM protein concentration, EB3 saturates the binding sites on growing microtubule plus ends but not on the lattice. Second, our previous single-molecule experiments showed that the association rates and dwell times of EB3 are significantly different when measured on the microtubule lattice and on the growing tips (Montenegro *et al.*, 2010), a conclusion that is supported by our FRAP data. Furthermore, we observed pronounced one-dimensional lattice diffusion for EB3 (Montenegro *et al.*, 2010), consistent with a transient and nonspecific electrostatic interaction mechanism. Third, in contrast to microtubule tip binding, we found that lattice binding is more sensitive to the ionic strength of the assay buffer used. This observation is in agreement with previous results showing that EB1 binds to the microtubule lattice through an electrostatic interaction between the positively charged CH domains and the negatively charged E-hooks of tubulin (Hayashi and Ikura, 2003; Zanic *et al.*, 2009; Maurer *et al.*, 2011). Fourth, the negatively charged nature of the C-terminal domain of EBs primarily suppresses microtubule lattice but not microtubule tip interaction.

It is believed that EBs might recognize a specific structural and/or chemical feature at the end of a growing microtubule (Sandblad *et al.*, 2006; des Georges *et al.*, 2008; Vitre *et al.*, 2008; Zanic *et al.*, 2009; Akhmanova and Steinmetz, 2011; Maurer *et al.*, 2011). Determining the microtubule end–bound structure of EBs and the nature of the EB-binding sites at growing microtubule tips is of utmost interest for the +TIP field. An immediate possible implication of the foregoing considerations is that the structural arrangement and binding mode of EB must be significantly different between the microtubule tip and lattice. In the latter case, our data suggest that several of the acidic residues of the C-terminal domain will be within a short distance from the negatively charged microtubule surface (Baker *et al.*, 2001). Only in this way can a meaningful long-range electrostatic repulsion that drives microtubule tip–binding specificity under physiological ionic strength conditions be achieved. In this model, the C-terminal domain is expected to be oriented alongside the microtubule lattice. In contrast, the interaction between EBs and microtubule tips seems not to be dominated by a long-range unspecific electrostatic component, since changes in solvent ionic strength and/or in the overall charge of the C-terminal domain do not significantly affect microtubule tip binding. In this case, the C-terminal domain is expected to be oriented away from the microtubule surface in such a manner as to avoid electrostatic repulsion. Alternatively, the electrostatic environment of the EB-binding sites at the microtubule tip is different from the lattice and thus allows for a favorable accommodation of the negatively charged C-terminal domain.

In conclusion, our data provide insights into the structural arrangement of EBs and some of the properties that EB-binding sites at microtubule tips must most likely encompass. The structural details and exact nature of the EB–microtubule tip interaction remain to be determined.

MATERIALS AND METHODS

Cloning and protein preparation

Human EB1, EB2, EB3, EB1ΔTail (residues 1–248), EB3ΔTail (residues 1–262), EB2ΔN (residues 44–328), EB1-NL (residues 1–189), EB1-NL-LZ, EB1-N-LZ (residues 1–136), and EB1-NL-LZ-Cort were cloned in pET3d (Novagen, EMD Biosciences, San Diego, CA) and expressed in BL21(DE3) (Invitrogen, Carlsbad, CA). EB1-NL-LZ, EB1-N-LZ, and EB1-NL-LZ-Cort were constructed by sequentially inserting into the pET3d-EB1 vector the leucine zipper (LZ) coiled-coil sequences of GCN4 (O'Shea *et al.*, 1991), the coiled-coil domain of cortexillin-1 (Steinmetz *et al.*, 1998), and a C-terminal 6xHis-tag using the CloneEZ PCR Cloning Kit (GenScript, Piscataway, NJ). GFP-EB3 and GFP-EB3ΔTail were described by Montenegro *et al.* (2010). EB3-NL-LZ-GFP was constructed by PCR substituting the native coiled coil and tail of the EB3 construct by the GCN4 leucine zipper (Komarova *et al.*, 2009).

Overexpressed proteins were purified by standard ion exchange (proteins without His-tag) or by immobilized metal affinity chromatography (proteins with His-tag) following standard chromatographic procedures. Proteins were further processed by size exclusion chromatography (SEC) in 20 mM Tris-HCl, 300 mM NaCl, pH 7.5, aliquoted, flash frozen in liquid nitrogen, and stored at −80°C until use. Shortly before the SAXS measurements, all proteins were processed by an additional SEC step, concentrated, and ultracentrifuged. The purity of the proteins, determined by densitometry on Coomassie-stained SDS–PAGE gels and mass spectrometry, was higher than 95% for all proteins.

Small-angle x-ray solution scattering

SAXS measurements were performed at the cSAXS beamline of the Swiss Light Source at the Paul Scherrer Institut, Villigen PSI, Switzerland. Buffer (20 mM Tris-HCl, 300 mM NaCl, 2 mM dithiothreitol, pH 7.5) and proteins (1–15 mg/ml) were measured at 10°C. Sixty frames were collected at 10 different capillary (1 mm diameter) positions with an exposure time of 0.25 s per frame.

SAXS data were processed using MATLAB (MathWorks, Natick, MA) scripts. Briefly, a mask was applied on each raw image to remove outliers (beam stop pixels, detector hot/cold pixels, etc.); the remaining pixels were radially averaged. In our setup the scattering vector ranged from ~0.01 to 0.6 $Å^{-1}$; however, only data out to 0.38 $Å^{-1}$ were used for further processing. All data frames were averaged after checking each measurement for radiation damage. Buffer scattering was subtracted, and the resulting spectra were normalized by its protein concentration and extrapolated to zero concentration. The radius of gyration was calculated by the Guinier approximation and from the pair-distribution function (PDF), as implemented in GNOM and AutoGNOM (Svergun, 1992). The maximum interatomic distance (D_{max}) was estimated from the PDF.

The low-resolution envelopes of the proteins were modeled ab initio (Supplemental Figures S3 and S4) using both a simulated annealing algorithm, implemented in the program DAMMIN (Svergun, 1999), and a genetic algorithm implemented in the program DALAI_GA (Chacón *et al.*, 2000). The independent results from the different programs agreed very well within the resolution limits of SAXS (20–30 Å; Supplemental Table S2). For each data set, at least 10 independent models were generated using DAMMIN or DALAI_GA. Models were superimposed and aligned in pairs with SUPCOMB (Kozin and Svergun, 2001). The most divergent ones were discarded, and the most probable structure was determined from the remaining models. The models with the lowest average spatial discrepancy were considered to be the most probable, whereas those with the highest ones were considered as outliers, according to previously established procedures (Volkov and Svergun, 2003). Next, the selected and aligned structures were averaged and filtered using DAMAVER and DAMFILT (Volkov and Svergun, 2003), respectively. The average excluded volume of DAMAVER was used as cut-off for DAMFILT. Atomic structures (Protein Data Bank [PDB] entries 1PA7 and 1WU9 for the CH and C-terminal domains of EB1, respectively) were manually docked into the SAXS-derived low-resolution maps using PYMOL (DeLano, 2002).

It should be noted that we did not find any evidence for a global symmetry in the SAXS data of all EB measurements. When we imposed P2 symmetry in DAMMIN, the twofold axis never coincided with the long axis of the two-stranded, parallel coiled coil, as it should be, but emerged at places without any physical meaning. However, the DAMMIN models without imposing symmetry perfectly fitted the DALAI_GA ones, further supporting the reliability of the asymmetric models (note that the program DALAI_GA does not allow one to impose symmetry).

The SAXS profiles of the isolated CH domain of EB1 was measured and analyzed as described. The experimental SAXS data are compatible with the theoretical profile calculated from the crystal structure (PDB entry 1PA7) of the EB1 CH domain (Supplemental Figure S1D) using the program CRYSOL (Svergun *et al.*, 1995).

Theoretical sedimentation coefficients of the SAXS-derived models were estimated using the software HYDRO++ (de la Torre *et al.*, 2007).

Chemical cross-linking and mass spectrometry

One hundred microliters of EB1 homodimer, EB3 homodimer, and EB1–EB3 heterodimer (1 mg/ml each) was cross-linked separately with 1 mM DSS (spacer length, 11.4 Å; Pierce, Thermo Fisher Scientific, Rockford, IL) in 20 mM sodium phosphate, 300 mM NaCl, pH 7.5, at 35°C for 30 min. The reaction was quenched by adding 50 mM Tris-HCl for 10 min at 35°C. Ten microliters of the resulting samples was analyzed by a 12% SDS–PAGE and found to be cross-linked (Supplemental Figure S6). As a negative control, a non–cross-linked EB1–EB3 heterodimer sample was used and processed as for the cross-linked proteins.

The protein samples were reduced with 1 mM Tris (2-carboxyethyl) phosphine hydrochloride (Pierce) at 37°C for 30 min and subsequently alkylated with 2 mM iodoacetamide (Sigma-Aldrich, St. Louis, MO) for 10 min at room temperature in the dark. For digestion 10% acetonitrile, urea (1 M final concentration), and 2% wt/wt trypsin (Promega, Madison, WI) were added. Digestion was carried out at 37°C overnight and stopped by acidification to 1% (wt/vol) trifluoroacetic acid. Peptides were purified with C18 MicroSpin columns (The Nest Group, Southborough, MA) and redissolved in 0.1% formic acid. Processing and liquid chromatography–MS/MS analysis was carried out on an LTQ Orbitrap XL mass spectrometer (Thermo Scientific) as described previously (Rinner *et al.*, 2008).

For data analysis we used xQuest, a software that was specifically developed to identify cross-linked peptides from MS/MS spectra (Rinner *et al.*, 2008). The MS/MS spectra were searched using xQuest's enumeration mode against a database containing the protein sequences of human EB1 and EB3. A precursor mass tolerance of 10 ppm was used. For matching of fragment ions, tolerances of 0.2 Da for common ions and 0.3 Da for cross-link ions were used. For monolinks a mass modification of 259.14197 Da for DSS-Tris (-1H) was included. All cross-linked peptides identified with a linear discriminant of >28.5 were considered for manual validation, where the identified MS/MS spectra were reviewed for matching ion series on both cross-linked peptide chains and for matching of the most abundant peaks. Experiments with standard proteins (Leitner *et al.*, 2010) showed that above this threshold the false-positive rate is <5%. The highest cross-link in the negative control sample reached a score of 14.5.

It should be noted that unambiguous identification of intersubunit cross-links within homodimers is usually not possible because they cannot be distinguished from intrasubunit ones. However, there is an exception in which both peptides of the cross-link share an identical and proteotypical sequence (i.e., a unique peptide for one protein that occurs only once in the sequence). Such a cross-link can only form between subunits within a homodimer.

Rotary metal shadowing and electron microscopy

Sample preparation and electron microscopy were according to Honnappa *et al.* (2005). Briefly, electron micrographs were taken in a Philips Morgagni TEM operated at 80 kV and equipped with a Megaview III charge-coupled device (CCD) camera. Protein samples (serial dilutions starting from 1 mg/ml) in buffer 20 mM Tris-HCl, 300 mM NaCl, pH 7.5, were supplemented with glycerol to a final concentration of 30%. The samples were subsequently sprayed onto freshly cleaved mica and rotary shadowed in a BA 511 M freeze-etch apparatus (Balzers, Lichtenstein) with platinum/carbon at an elevation angle of 3–5°.

For image analysis, we followed the procedure used to average the head domain of the Ndc80 complex (Wang *et al.*, 2008). Two hundred forty-nine electron micrographs of individual EB1-NL-LZ-Cort dimers, including heads and parts of the coiled-coil rod domain, were extracted by X3dpreprocess (Conway and Steven, 1999). Extracted images were subsequently classified by the K-means clustering algorithm into 20 subclasses, and subaverages were calculated using SPIDER (Frank *et al.*, 1996).

In vitro microtubule tip–tracking assay and analysis of fluorescence intensities on microtubule tips and lattices

Reconstitution of plus end tracking in vitro was performed as described by Montenegro *et al.* (2010). Briefly, microtubules were

grown at 30°C in the presence of 15 μM tubulin and different purified GFP-EB3 fusions from GMPCPP-stabilized, rhodamine-labeled microtubule seeds that were immobilized on coverslips using biotin–streptavidin links. The assay buffer contained 80 mM 1,4-piperazinediethanesulfonic acid (PIPES), 4 mM $MgCl_2$, 1 mM ethylene glycol tetraacetic acid (EGTA), pH adjusted to 6.8 with KOH, and was supplemented with 15 μM bovine brain tubulin (Cytoskeleton, Denver, CO), 50 or 65 mM KCl, 1 mM GTP, 0.2 mg/ml κ-casein, and 0.1% methylcellulose. Images were collected using total internal reflection fluorescence microscopy (TIRFM), which was performed on an inverted research microscope, Nikon Eclipse Ti-E (Nikon, Melville, NY), equipped with a Perfect Focus System (Nikon), a TIRF-E motorized TIRF illuminator, modified by Roper Scientific (La Petite Montagne Sud, France) and the Cell and Tissue Imaging Facility, Curie Institute (PICT-IBiSA; Paris, France) for the attachment of the FRAP system, with a CFI Apo TIRF 100× 1.49–numerical aperture oil objective (Nikon), with a QuantEM 512SC electron-multiplying CCD camera (Roper Scientific), and controlled by MetaMorph 7.5 software (Molecular Devices, Sunnyvale, CA). For excitation we used a 50-mW, 491-nm Calypso diode-pumped solid-state laser (Cobolt, Solna, Sweden) and a 50-mW, 561-nm Jive diode-pumped solid-state laser (Cobolt) in combination with a Chroma Technology (Bellows Falls, VT) ET-GFP/mCherry filter cube. The 16-bit images were projected onto the CCD chip with 2.5× intermediate lens (Nikon C mount adapter 2.5×) at a magnification of 0.065 μm/pixel. The I-Las/I-Launch FRAP scanning system (Roper Scientific/PICT-IBiSA) was used for carrying out the FRAP assay.

Measurement of fluorescence intensities of microtubule tips and tip-to-lattice ratios was performed using kymographs with background subtraction. The average intensity of GFP-EB3 and mutants for individual growth events was measured in the green channel using a 10–pixel-wide line. The same regions were then transferred to the corresponding region of fresh microtubule lattice, where the tip-to-lattice ratio was expressed as the tip intensity divided by the lattice intensity. Microtubule dynamics parameters were determined using kymographs as described by Montenegro *et al.* (2010).

FRAP analysis of protein turnover on microtubules in vitro

FRAP was performed on an inverted research microscope, Nikon Eclipse Ti-E (Nikon), described earlier. For studying the fluorescence recovery of EB3-GFP and its mutants at the microtubule ends we performed imaging of full 512 × 512 pixel frames at 5 or 33 frames/s for 15–30 s. During the imaging we bleached EB3 comets or lattice regions using the FRAP-on-fly option (Roper Scientific/PICT-IBiSA). The FRAP-on-fly option allows bleaching of a circular image region 0.5 μm in diameter selected by the position of a mouse cursor. We used 100% of the laser power for photobleaching.

For analysis, we chose the comets or lattice regions that were effectively bleached and plotted a kymograph along these microtubules. Fluorescence recovery in the comets was analyzed in the region that had the highest fluorescence intensity at the last time point before photobleaching. The measured image intensities over time from the bleached (at time t_0) region were given by a set of T measurements $y^*_{FRAP} = \{y_1,\ldots,y_{t_0},\ldots,y_T\}$. The recovery of fluorescence was modeled as $y_{FRAP}(t) = \{1 - \exp[-b(t - t_0)]\}y_0(t)$ for $t > t_0$, where $y_0(t)$ describes the corresponding intensity distribution for the same (but nonbleached) region of microtubule. However, in practice, it was not possible to measure $y_0(t)$ for the same microtubule. To estimate −b (which represents k_{off} in the current model), we used an approximation of the nonbleached comet intensity distribution $y_0(t)$ as $y_0(t) = A\exp[-a(t - t_0)] + B$, where the parameters A, B, and a were estimated using the least squares fitting and 5–10 measurements from the curve $y_{FRAP}(t)$ just before the bleaching (time t_0), $\{y_{t_0-5},\ldots,y_{t_0}\}$, and 10–20 intensity measurements from the end of the curve $y_{FRAP}(t)$, $\{y_{T-20},\ldots,y_T\}$. Having such an estimate of the nonbleached comet intensity, we applied log transform to $y_{FRAP}(t)$ and obtained the equation $-b(t - t_0) = \log|1 - y_{FRAP}(t)/y_0(t)|$. By plotting the right-hand side of this equation [where $y_{FRAP}(t) = y^*_{FRAP}$ and $t = \{t_0,\ldots,t_T\}$] and using the linear regression, we estimated the slope of the resulting curve, which corresponded to b. Residence time was calculated as −1/b. The same algorithm was applied to the microtubule lattice, to make the measurements directly comparable. Fluorescence recovery on the lattice was measured in the middle of the photobleached region.

Microtubule polymerization and pelleting assays

The kinetics of tubulin (25 μM) assembly at 37°C in the presence of different EB proteins (12.5 μM monomer equivalents) was monitored by DAPI fluorescence emission at 450 nm in 80 mM PIPES-KOH, 4 mM $MgCl_2$, 1 mM EGTA, 1 mM GTP, pH 6.8, as previously described (Bonne *et al.*, 1985) using a Tecan (Männedorf, Switzerland) Ultra Evolution fluorescence plate reader.

The amounts of polymers induced by different EB1 proteins and the amounts of EB1 proteins bound to the microtubule lattice were confirmed and assessed, respectively, by microtubule pelleting experiments (Supplemental Figure S8). For monitoring formation of microtubules in the presence of EB1 proteins, 25 μM tubulin was polymerized in the presence of 12.5 μM EB protein variants in buffer 80 mM PIPES-KOH, 4 mM $MgCl_2$, 1 mM EGTA, 1 mM GTP, pH 6.8. Samples were incubated at 37°C for 45 min and centrifuged at 37°C at 100,000 × *g* for 10 min. Supernatants and pellets were subsequently analyzed by Coomassie-stained SDS–PAGE. To determine the amount of EB1 proteins bound to the microtubule lattice, 15 μM tubulin was polymerized in the presence of equimolecular amounts of Taxol and the EB1 protein variants in buffer 30% (vol/vol) glycerol, 80 mM PIPES, 1 mM EGTA, 4 mM $MgCl_2$, 1 mM GTP, pH 6.8, at 30°C for 20 min. Samples were centrifuged at 30°C for 30 min at 21,000 × *g*. Pellets and supernatants were analyzed by SDS–PAGE. Band intensities were quantified with ImageJ (National Institutes of Health, Bethesda, MD) by drawing rectangular regions of equal size around each band.

ACKNOWLEDGMENTS

We are indebted to T. Ishikawa for help with the image processing, to V. Olivieri and G. Morson (Center for Microscopy, University of Basel, Basel, Switzerland) for excellent technical support and access to the electron microscope, and to F. Diaz, M. Balsera, M. Beck, O. Rinner, A. Leitner, C. Moores, and F. Winkler for insightful discussions. This work was supported by a long-term Federation of European Biochemical Societies fellowship and a contract from the Juan de la Cierva program (to R.M.B.), by funding from the European Union 7th Framework Program PROSPECTS (to T.W. and R.A.), by a grant from the Swiss National Science Foundation (to M.O.S.), by a European Molecular Biology Organization Long Term Fellowship (to R. M.), and by a Netherlands Organisation for Scientific Research, Earth and Life Sciences, Vici Grant (to A.A).

REFERENCES

Akhmanova A, Steinmetz MO (2008). Tracking the ends: a dynamic protein network controls the fate of microtubule tips. Nat Rev Mol Cell Biol 9, 309–322.

Akhmanova A, Steinmetz HO (2011). Microtubule end binding: EBs sense the guanine nucleotide state. Curr Biol 21, R283–R285.

Baker NA, Sept D, Joseph S, Holst MJ, McCammon JA (2001). Electrostatics of nanosystems: application to microtubules and the ribosome. Proc Natl Acad Sci USA 98, 10037–10041.
Bieling P, Kandels-Lewis S, Telley IA, van Dijk J, Janke C, Surrey T (2008). CLIP-170 tracks growing microtubule ends by dynamically recognizing composite EB1/tubulin-binding sites. J Cell Biol 183, 1223–1233.
Bieling P, Laan L, Schek H, Munteanu EL, Sandblad L, Dogterom M, Brunner D, Surrey T (2007). Reconstitution of a microtubule plus-end tracking system in vitro. Nature 450, 1100–1105.
Bonne D, Heusele C, Simon C, Pantaloni D (1985). 4′,6-Diamidino-2-phenylindole, a fluorescent probe for tubulin and microtubules. J Biol Chem 260, 2819–2825.
Chacón P, Díaz JF, Morán F, Andreu JM (2000). Reconstruction of protein form with x-ray solution scattering and a genetic algorithm. J Mol Biol 299, 1289–1302.
Ciferri C *et al.* (2008). Implications for kinetochore-microtubule attachment from the structure of an engineered Ndc80 complex. Cell 133, 427–439.
Conway JF, Steven AC (1999). Methods for reconstructing density maps of "single" particles from cryoelectron micrographs to subnanometer resolution. J Struct Biol 128, 106–118.
De Groot CO *et al.* (2010). Molecular insights into mammalian end-binding protein heterodimerization. J Biol Chem 285, 5802–5814.
de la Torre JG, Echenique GR, Ortega A (2007). Improved calculation of rotational diffusion and intrinsic viscosity of bead models for macromolecules and nanoparticles. J Phys Chem B 111, 955–961.
DeLano WL (2002). The PyMOL Molecular Graphics System, Palo Alto, CA: DeLano Scientific.
des Georges A, Katsuki M, Drummond DR, Osei M, Cross RA, Amos LA (2008). Mal3, the *Schizosaccharomyces pombe* homolog of EB1, changes the microtubule lattice. Nat Struct Mol Biol 15, 1102–1108.
Dougherty GW, Adler HJ, Rzadzinska A, Gimona M, Tomita Y, Lattig MC, Merritt RC Jr, Kachar B (2005). CLAMP, a novel microtubule-associated protein with EB-type calponin homology. Cell Motil Cytoskeleton 62, 141–156.
Dragestein KA, van Cappellen WA, van Haren J, Tsibidis GD, Akhmanova A, Knoch TA, Grosveld F, Galjart N (2008). Dynamic behavior of GFP-CLIP-170 reveals fast protein turnover on microtubule plus ends. J Cell Biol 180, 729–737.
Frank J, Radermacher M, Penczek P, Zhu J, Li Y, Ladjadj M, Leith A (1996). SPIDER and WEB: processing and visualization of images in 3D electron microscopy and related fields. J Struct Biol 116, 190–199.
Galjart N (2010). Plus-end-tracking proteins and their interactions at microtubule ends. Curr Biol 20, R528–R537.
Gimona M, Djinovic-Carugo K, Kranewitter WJ, Winder SJ (2002). Functional plasticity of CH domains. FEBS Lett 513, 98–106.
Hayashi I, Ikura M (2003). Crystal structure of the amino-terminal microtubule-binding domain of end-binding protein 1 (EB1). J Biol Chem 278, 36430–36434.
Hayashi I, Wilde A, Mal TK, Ikura M (2005). Structural basis for the activation of microtubule assembly by the EB1 and p150Glued complex. Mol Cell 19, 449–460.
Honnappa S *et al.* (2009). An EB1-binding motif acts as a microtubule tip localization signal. Cell 138, 366–376.
Honnappa S, John CM, Kostrewa D, Winkler FK, Steinmetz MO (2005). Structural insights into the EB1-APC interaction. EMBO J 24, 261–269.
Howard J, Hyman AA (2003). Dynamics and mechanics of the microtubule plus end. Nature 422, 753–758.
Jura N, Endres NF, Engel K, Deindl S, Das R, Lamers MH, Wemmer DE, Zhang X, Kuriyan J (2009). Mechanism for activation of the EGF receptor catalytic domain by the juxtamembrane segment. Cell 137, 1293–1307.
Komarova Y *et al.* (2009). Mammalian end binding proteins control persistent microtubule growth. J Cell Biol 184, 691–706.
Komarova Y, Lansbergen G, Galjart N, Grosveld F, Borisy GG, Akhmanova A (2005). EB1 and EB3 control CLIP dissociation from the ends of growing microtubules. Mol Biol Cell 16, 5334–5345.
Kozin MB, Svergun DI (2001). Automated matching of high- and low-resolution structural models. J Appl Crystallogr 34, 33–41.
Leitner A, Walzthoeni T, Kahraman A, Herzog F, Rinner O, Beck M, Aebersold R (2010). Probing native protein structures by chemical cross-linking, mass spectrometry and bioinformatics. Mol Cell Proteomics 9, 1634–1649.
Ligon LA, Shelly SS, Tokito M, Holzbaur EL (2003). The microtubule plus-end proteins EB1 and dynactin have differential effects on microtubule polymerization. Mol Biol Cell 14, 1405–1417.
Manna T, Honnappa S, Steinmetz MO, Wilson L (2008). Suppression of microtubule dynamic instability by the +TIP protein EB1 and its modulation by the CAP-Gly domain of p150(Glued). Biochemistry 47, 779–786.
Maurer SP, Bieling P, Cope J, Hoenger A, Surrey T (2011). GTPγS microtubules mimic the growing microtubule end structure recognized by end-binding proteins (EBs). Proc Natl Acad Sci USA 108, 3988–3993.
Montenegro GS *et al.* (2010). In vitro reconstitution of the functional interplay between MCAK and EB3 at microtubule plus ends. Curr Biol 20, 1717–1722.
O'Shea EK, Klemm JD, Kim PS, Alber T (1991). X-ray structure of the GCN4 leucine zipper, a two-stranded, parallel coiled coil. Science 254, 539–544.
Rinner O, Seebacher J, Walzthoeni T, Mueller LN, Beck M, Schmidt A, Mueller M, Aebersold R (2008). Identification of cross-linked peptides from large sequence databases. Nat Methods 5, 315–318.
Sandblad L, Busch KE, Tittmann P, Gross H, Brunner D, Hoenger A (2006). The *Schizosaccharomyces pombe* EB1 homolog Mal3p binds and stabilizes the microtubule lattice seam. Cell 127, 1415–1424.
Schuyler SC, Pellman D (2001). Microtubule "plus-end-tracking proteins": the end is just the beginning. Cell 105, 421–424.
Seebacher J, Mallick P, Zhang N, Eddes JS, Aebersold R, Gelb MH (2006). Protein cross-linking analysis using mass spectrometry, isotope-coded cross-linkers, and integrated computational data processing. J Proteome Res 5, 2270–2282.
Skube SB, Chaverri JM, Goodson HV (2010). Effect of GFP tags on the localization of EB1 and EB1 fragments in vivo. Cytoskeleton (Hoboken) 67, 1–12.
Slep KC (2010). Structural and mechanistic insights into microtubule end-binding proteins. Curr Opin Cell Biol 22, 88–95.
Slep KC, Rogers SL, Elliott SL, Ohkura H, Kolodziej PA, Vale RD (2005). Structural determinants for EB1-mediated recruitment of APC and spectraplakins to the microtubule plus end. J Cell Biol 168, 587–598.
Slep KC, Vale RD (2007). Structural basis of microtubule plus end tracking by XMAP215, CLIP-170, and EB1. Mol Cell 27, 976–991.
Steinmetz MO, Stock A, Schulthess T, Landwehr R, Lustig A, Faix J, Gerisch G, Aebi U, Kammerer RA (1998). A distinct 14 residue site triggers coiled-coil formation in cortexillin I. EMBO J 17, 1883–1891.
Su LK, Qi Y (2001). Characterization of human MAPRE genes and their proteins. Genomics 71, 142–149.
Svergun DI (1992). Determination of the regularization parameter in indirect-transform methods using perceptual criteria. J Appl Crystallogr 25, 495–503.
Svergun DI (1999). Restoring low resolution structure of biological macromolecules from solution scattering using simulated annealing. Biophys J 76, 2879–2886.
Svergun DI, Barberato C, Koch MHJ (1995). CRYSOL—a program to evaluate x-ray solution scattering of biological macromolecules from atomic coordinates. J Appl Crystallogr 28, 768–773.
Vitre B, Coquelle FM, Heichette C, Garnier C, Chretien D, Arnal I (2008). EB1 regulates microtubule dynamics and tubulin sheet closure in vitro. Nat Cell Biol 10, 415–421.
Volkov VV, Svergun DI (2003). Uniqueness of ab initio shape determination in small-angle scattering. J Appl Crystallogr 36, 860–864.
Wang HW, Long S, Ciferri C, Westermann S, Drubin D, Barnes G, Nogales E (2008). Architecture and flexibility of the yeast Ndc80 kinetochore complex. J Mol Biol 383, 894–903.
Zanic M, Stear JH, Hyman AA, Howard J (2009). EB1 recognizes the nucleotide state of tubulin in the microtubule lattice. PLoS One 4, e7585.
Zhu ZC, Gupta KK, Slabbekoorn AR, Paulson BA, Folker ES, Goodson HV (2009). Interactions between EB1 and microtubules: dramatic effect of affinity tags and evidence for cooperative behavior. J Biol Chem 284, 32651–32661.
Zimniak T, Stengl K, Mechtler K, Westermann S (2009). Phosphoregulation of the budding yeast EB1 homologue Bim1p by Aurora/Ipl1p. J Cell Biol 186, 379–391.